

1 Supplementary material

2 S1. True depth resolution of the CFA records

3 Depth resolution of the CFA records have been evaluated based on the time it took for the
4 various CFA measurement lines to transition from a blank water standard to a calibration
5 standard plateau. Response times were evaluated in terms of the average time required for the
6 system to transition from 10% to 90% of the highest calibration standard level (Table S1).
7 With the employed melt rate of 3 cm min^{-1} , these response times can be converted to
8 equivalent response depths, which provide a measure for the true depth resolution of the
9 employed CFA system for the various measurement lines and analytical systems. For the
10 RICE CFA set-up, conductivity is the highest resolution record with a response depth of 0.8
11 cm.

12

	Response time (s)	Response depth (cm)
Conductivity	15 ± 2	0.8 ± 0.1
Acidity	38 ± 3	1.9 ± 0.2
Calcium	49 ± 6	2.4 ± 0.3
Black carbon	20 ± 3	1.0 ± 0.2

13

14 **Table S1:** Response time for the CFA system to transition from a 10% to 90% of the
15 difference between the blank water level and a calibration standard plateau, and the equivalent
16 response depths.

17

18 S2. StratiCounter settings and procedure

19 Slight changes in the StratiCounter settings with depth were required due to the rapid thinning
20 of layers with depth. We therefore divided the ice-core records into four sections: an upper
21 (42.5-180 m), an upper middle (165-250 m), a lower middle (240-300 m), and a lower section
22 (280-344 m). Overlap sections served as base for comparison between the runs, which were
23 found to contain only minor differences. Within the overlap sections, the results from the
24 deeper section were used to produce the final timescale.

25 For all sections, the algorithm was run using the same data set, except that the dust record was
26 excluded for the three lowermost sections due to its contamination. The main difference
27 between the four sections was the averaging distance employed to produce a lower-resolution
28 record from the original 1 mm resolution CFA records, performed before automatic layer
29 counting. Section delimitations were selected based on estimated layer thicknesses obtained
30 from methane matching to WAIS Divide ice core (section 3.2.6), and chosen so that an
31 average layer consists of approximately 10-15 individual data points. Accordingly, the
32 averaging distance was successively reduced from 1.5 cm to 0.5 cm to account for the general
33 decrease in layer thicknesses with depth (Table S2). Note that the averaging distance applied
34 for the deepest section is less than the estimated true resolution of even the highest-resolution
35 impurity records (Table S1), meaning that successive averaged data points are significantly

1 correlated. At 344 m, where the annual layer-counted timescale stops, the average layer
 2 thickness is 6 cm.

3
 4

Impurity series	42-180 m	160-250 m	240 – 300 m	280-350 m
Black carbon	1	1	1	1
Acidity	0.5	0.5	0.5	0.5
Dust	0.5	0	0	0
Calcium	0.25	0.25	0.25	0.25
Conductivity	0.25	0.25	0.25	0.25
Depth resolution of data series (cm)	1.5	1.0	0.7	0.5

5 **Table S2:** *StratiCounter* relative weightings of data series for each depth range. The algorithm
 6 settings were slightly adjusted for the three depth intervals, as necessitated by reduced layer
 7 thicknesses with depth and contamination of the dust record below 130m.

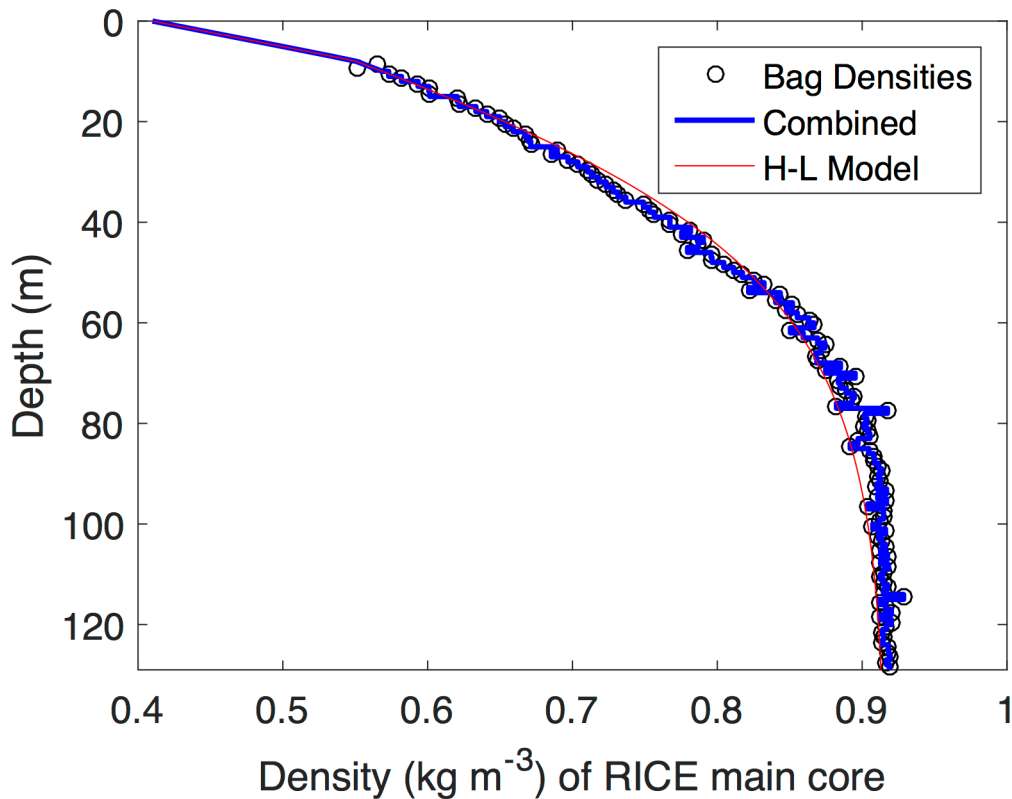
8 *StratiCounter* was run based on the full suite of CFA records: BC, acidity, dust, calcium, and
 9 conductivity records. Before analysis, outliers in the form of extreme peaks caused by
 10 measurement noise and processing errors were removed from the data series, and,
 11 additionally, the annual signal in the data was made more regular by taking the logarithm to
 12 the data. For the lower three sections, however, the dust record was contaminated, and
 13 therefore excluded from the analysis. Including this noisy data series in the 130-160 m section
 14 did not influence the performance of the algorithm, probably because the resulting timescale
 15 was dominated by the much stronger annual signal in the remaining data series, and especially
 16 the black carbon record.

17 Black carbon had the most reliable annual signal, and this record was weighted highest. The
 18 acidity and dust (when included) records were each weighted half as much as the signal in the
 19 black carbon record. Similar weightings were given to the combined calcium/conductivity
 20 records, while accounting for the very high degree of similarity between the two records
 21 (Kjær et al., 2016) (Table S2).

22
 23
 24
 25
 26
 27
 28

1
2
3

S3. Density profile, modelled and observed



4

5 *Figure S1: Measured and modelled density profiles for the RICE core.*

6 The density profile used in RICE timescale calculations was based upon a combination of
7 measured and modeled data. We chose an initial density of 0.41 g cm^{-3} , a surface temperature
8 of -22° C , and an accumulation rate of $0.22 \text{ m w.e yr}^{-1}$, which provided a good fit to the
9 observed density profile (Fig. S1). The value chosen for the initial density was within the
10 range of measured snow density from adjacent snow pits, while the surface temperature was a
11 few degrees warmer than that implied by ERAi reanalyses and borehole temperature
12 measurements (Bertler et al., 2017). The small differences between observed and modelled
13 density profiles may indicate that the density profile is not in steady state, or it might be due
14 to the additional vertical strain present at divide locations (Kingslake et al., 2014).

15

16 S4. Seasonality of impurity influx to Roosevelt Island

17 Using the annual layer-counted RICE17 timescale, we can quantify the seasonal variability of
18 impurity influx to Roosevelt Island visible in the ice core records. We describe the annual
19 signals observed in the five RICE CFA records: black carbon, acidity, calcium, conductivity
20 and insoluble particles (dust). Figure S2 shows the averaged seasonal pattern of each of these
21 records for three different time intervals.

22

1 **S4.1 Sulfur and acidity**

2 Sulfur-containing compounds have a variety of sources, one of which is dimethylsulfide
3 (DMS) emissions by phytoplankton activity during summer (Legrand et al., 1991; Udisti et
4 al., 1998). At times, however, annual signals in the IC sulfate (SO_4^{2-}) and ICP-MS sulfur (S)
5 records were ambiguous as they occasionally displayed large sulfur peaks caused by extreme
6 sea-salt influx events. Improved annual-layer identification was obtained by using measured
7 sodium concentrations to calculate the non-sea-salt-sulfate (nssSO_4^{2-}) and non-sea-salt-sulfur
8 (nssS) fractions. Non-sea-salt sulfur-containing compounds drive most of the variability in the
9 continuously-measured CFA acidity record (Kjær et al. 2016), which similarly displays a very
10 regular annual signal. Most of the RICE CFA records, however, suffered from several data
11 gaps in the topmost part of the core.

12 The seasonality of acidity is effectively the inverse of sea salt, with a minimum in late
13 winter/spring and a maximum in January/February – late summer. At Law Dome, a
14 January/February peak of MSA (an oxidative product of marine biogenically-produced DMS)
15 is observed, with a minimum in August/September. The high correspondence between acidity
16 and non-sea-salt sulfate (measured by IC) in the top part of the core shows that the acidity
17 variation is a response to the sulfuric acidity content in the ice, which (if disregarding the non-
18 annual influx of volcanic sulfate) is another byproduct of the marine biogenic input. For
19 comparison, at WAIS divide, the annual signal of nssS peaks in March/April, two months
20 later than observed at RICE (Sigl et al., 2016).

22 **S4.2 Iodine**

23 Iodine concentrations also showed a very regular annual signal, peaking in winter with an
24 average peak value around 1000 ppb. Atmospheric iodine concentrations in coastal Antarctica
25 are attributed to biological activity in sea ice. While this activity is highest in summer,
26 photolysis of snowpack iodine during the summer months leads to the highest concentrations
27 of iodine in the winter snow (Frieß et al., 2010). As a result of this complex process, not all
28 winters have a clear expression in the RICE iodine records, but high concentrations do not
29 occur during summertime.

30 **S4.3 Sea-salt derived species**

31 Several other records also display annual variability, but with a much more irregular signal.
32 Sodium (IC), calcium (CFA, IC) and other sea-salt-derived impurities usually peak during
33 summer, but oftentimes have multiple peaks per year. The CFA dust record was very noisy in
34 this top part of the core. The seasonality of conductivity and calcium closely follow each
35 other, and are representative of the annual signal in sea salts deposited at Roosevelt Island.
36 For calcium, we observe a late winter/spring peak in the typical year. This calcium peak is
37 located a few months later than the corresponding sea salt peak (Na) in the WAIS Divide ice
38 core. For the deeper sections, this annual signal is indistinguishable from the inter-annual
39 variability.

40 **S4.4 Black carbon**

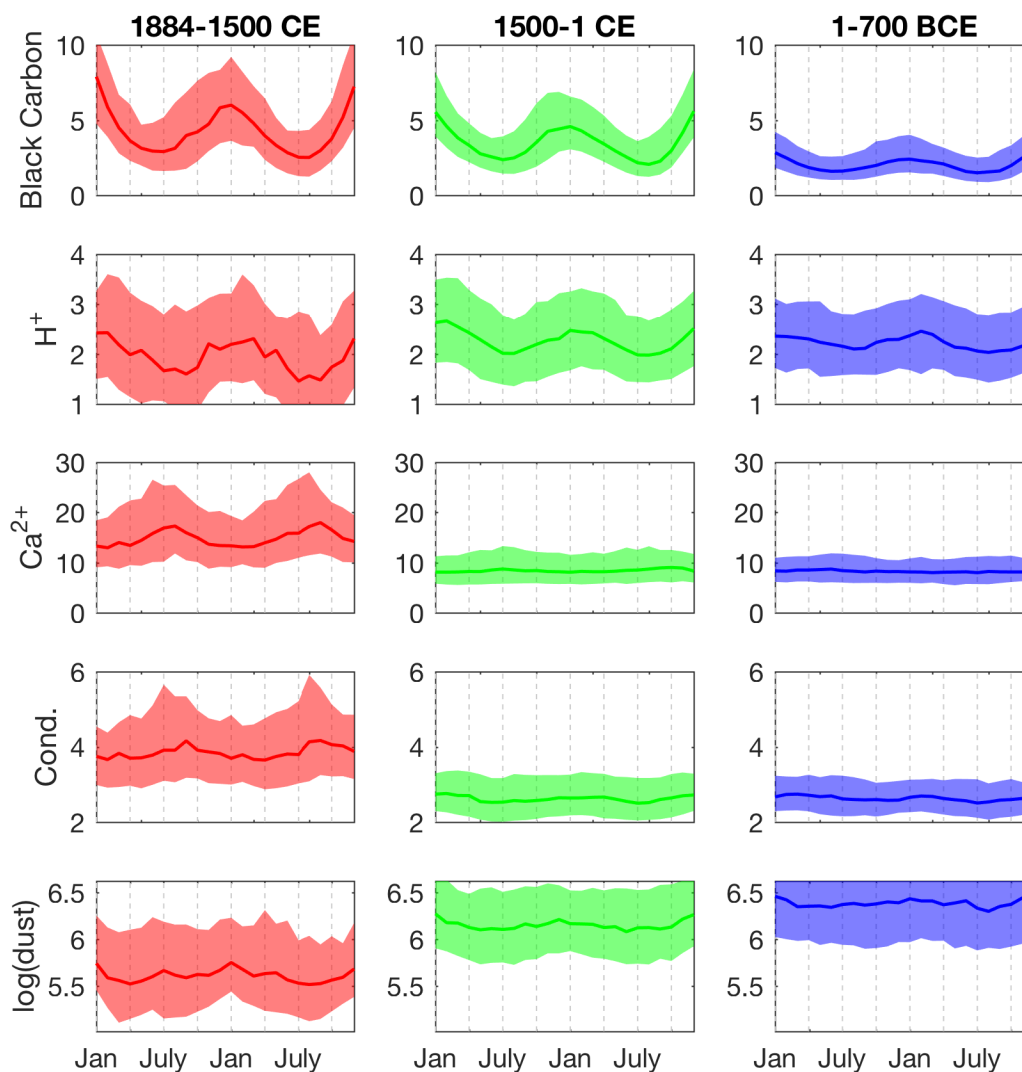
41 The seasonal deposition of black carbon (BC) in Antarctic snow is primarily driven by
42 biomass burning emissions in the Southern Hemisphere (Bisiaux et al., 2012), which peak
43 during the late austral spring/summer (Bauer et al., 2013; Lamarque et al., 2010). Southern
44 Hemisphere fossil fuel emissions have increased since the 1950's (Lamarque et al., 2010).
45 However, they are still thought to be a minor component of seasonal BC emissions (Bauer et
46 al., 2013). Decadal-scale decreases in biomass burning emissions or/and changes in long-
47 range atmospheric transport impact the fidelity of the seasonal peak, and its usefulness for

1 annual layer counting. For example, the ice-core BC seasonality was more pronounced before
2 the 20th century, and its annual signal in the top part of the RICE core was not as clear as, e.g.
3 that of the sulfate and acidity records. The timing of the BC peak is also likely to shift from
4 location to location and due to seasonal differences in atmospheric circulation. At RICE BC
5 displays a clear Austral mid-summer peak, which we here assume to be in December/January,
6 and a minimum in Austral winter. We note that this summer peak occurs earlier than in the
7 WAIS Divide core, where it was found to peak in April (Sigl et al., 2016). With increasing
8 depth, the annual signal is reduced, but in terms of level, amplitude, and inter-annual
9 variability, but the amplitude of the seasonal cycle remains significant to great depths. Even
10 in the lower-most section of the timescale (blue), the seasonal cycle is visible, although inter-
11 annual variability (“noise”) here is starting to become of similar magnitude as the seasonal
12 variability, meaning that the data is starting to become marginal for reliable annual-layer
13 identification.

14 **S4.5 Dust**

15 The seasonal pattern of insoluble particles (dust) resembles that of BC, although the seasonal
16 pattern here is not very pronounced. It peaks in summer, and from the range of inter-annual
17 variability, we can see that it does so during most summers. However, the variability is very
18 high, and peaks may also occur at other times of the year. Below 129 m, the record was
19 contaminated, and the annual signal is lost. The simultaneous deposition of black carbon and
20 dust is consistent with the two chemistry tracers arriving via long-range transport of both
21 parameters from the continents of the southern hemisphere. Other support for spring/summer
22 as the primary seasons for intercontinental transport of aerosols to Antarctica are shown by
23 September-December peak of lead (Pb) concentrations in high-resolution firn cores from
24 West Antarctica (McConnell et al., 2014) and lower-resolution measurements of Pb and Ba in
25 Law Dome ice cores (Burn-Nunes et al., 2011).

26



1
2
3
4
5
6
7
8

Figure S2: Annual signals of 2 successive years in the five RICE CFA chemistry series: black carbon, acidity (H⁺), calcium (Ca²⁺), conductivity (Cond.), and insoluble dust particles (dust, log. scale) for three different time periods. The line shows the monthly-averaged median value of the measured concentration, and colored area signifies the 25% and 75% quantile envelope of the averaged value distribution.

9 **Supplementary references**

10 Bauer, S. E., Bausch, A., Nazarenko, L., Tsigaridis, K., Xu, B., Edwards, R., Bisiaux, M., and
 11 McConnell, J.: Historical and future black carbon deposition on the three ice caps: Ice core
 12 measurements and model simulations from 1850 to 2100, *J. Geophys. Res. Atmos.*, 118,
 13 7948-7961, doi: 10.1002/jgrd.50612, 2013.

14 Bertler, N. A. N., Conway, H., Dahl-Jensen, D., Emanuelsson, D. B., Winstrup, M.,
 15 Vallelonga, P. T., Lee, J. E., Brook, E. J., Severinghaus, J. P., Fudge, T. J., Keller, E. D.,
 16 Baisden, W. T., Hindmarsh, R. C. A., Neff, P. D., Blunier, T., Edwards, R., Mayewski, P. A.,

- 1 Kipfstuhl, S., Buizert, C., Canessa, S., Dacic, R., Kjær, H. A., Kurbatov, A., Zhang, D.,
2 Waddington, E. D., Baccolo, G., Beers, T., Brightley, H. J., Carter, L., Clemens-Sewall, D.,
3 Ciobanu, V. G., Delmonte, B., Eling, L., Ellis, A. A., Ganesh, S., Golledge, N. R., Haines, S.
4 A., Handley, M., Hawley, R. L., Hogan, C. M., Johnson, K. M., Korotkikh, E., Lowry, D. P.,
5 Mandeno, D., McKay, R. M., Menking, J. A., Naish, T. R., Noerling, C., Ollive, A., Orsi, A.,
6 Proemse, B. C., Pyne, A. R., Pyne, R. L., Renwick, J., Scherer, R. P., Semper, S., Simonsen,
7 M., Sneed, S. B., Steig, E. J., Tuohy, A., Ulayottil Venugopal, A., Valero-Delgado, F.,
8 Venkatesh, J., Wang, F., Wang, S., Winski, D. A., Winton, V. H. L., Whiteford, A., Xiao, C.,
9 Yang, J., and Zhang, X.: The Ross Sea Dipole - Temperature, Snow Accumulation and Sea
10 Ice Variability in the Ross Sea Region, Antarctica, over the Past 2,700 Years, *Clim. Past*
11 *Discuss.*, 2017, 1-31, doi: 10.5194/cp-2017-95, 2017.
- 12 Bisiaux, M. M., Edwards, R., McConnell, J. R., Curran, M. A. J., Van Ommen, T. D., Smith,
13 A. M., Neumann, T. A., Pasteris, D. R., Penner, J. E., and Taylor, K.: Changes in black
14 carbon deposition to Antarctica from two high-resolution ice core records, 1850, Åi2000 AD,
15 *Atmos. Chem. Phys.*, 12, 4107-4115, doi: 10.5194/acp-12-4107-2012, 2012.
- 16 Burn-Nunes, L. J., Vallelonga, P., Loss, R. D., Burton, G., Moy, A., Curran, M., Hong, S.,
17 Smith, A. M., Edwards, R., Morgan, V., and Rosman, K. J. R.: Seasonal variability in the
18 input of lead, barium and indium to Law Dome, Antarctica, *Geochim. Cosmochim. Acta*, 75,
19 1-20, doi: 10.1016/j.gca.2010.09.037, 2011.
- 20 Frieß, U., Deutschmann, T., Gilfedder, B. S., Weller, R., and Platt, U.: Iodine monoxide in the
21 Antarctic snowpack, *Atmos. Chem. Phys.*, 10, 2439-2456, doi: 10.5194/acp-10-2439-2010,
22 2010.
- 23 Kingslake, J., Hindmarsh, R. C. A., Aðalgeirsdóttir, G., Conway, H., Corr, H. F. J., Gillet-
24 Chaulet, F., Martín, C., King, E. C., Mulvaney, R., and Pritchard, H. D.: Full-depth englacial
25 vertical ice sheet velocities measured using phase-sensitive radar, *Journal of Geophysical*
26 *Research: Earth Surface*, 119, 2604-2618, doi: 10.1002/2014JF003275, 2014.
- 27 Kjær, H. A., Vallelonga, P., Svensson, A., Elleskov L. Kristensen, M., Tibuleac, C.,
28 Winstrup, M., and Kipfstuhl, S.: An Optical Dye Method for Continuous Determination of
29 Acidity in Ice Cores, *Environ. Sci. Technol.*, doi: 10.1021/acs.est.6b00026, 2016.
- 30 Lamarque, J. F., Bond, T. C., Eyring, V., Granier, C., Heil, A., Klimont, Z., Lee, D., Liousse,
31 C., Mieville, A., Owen, B., and Schultz, M. G.: Historical (1850–2000) gridded
32 anthropogenic and biomass burning emissions of reactive gases and aerosols: methodology
33 and application, *Atmos. Chem. Phys.*, 10, 7017-7039, doi: 10.5194/acp-10-7017-2010, 2010.
- 34 Legrand, M., Feniet-Saigne, C., Saltzman, E. S., Germain, C., Barkov, N. I., and Petrov, V.
35 N.: Ice-core record of oceanic emissions of dimethylsulphide during the last climatic cycle,
36 *Nature*, 350, 144-146, doi: 10.1038/350144a0, 1991.
- 37 McConnell, J. R., Maselli, O. J., Sigl, M., Vallelonga, P., Neumann, T., Anschütz, H., Bales,
38 R. C., Curran, M. A. J., Das, S. B., Edwards, R., Kipfstuhl, S., Layman, L., and Thomas, E.
39 R.: Antarctic-wide array of high-resolution ice core records reveals pervasive lead pollution
40 began in 1889 and persists today, *Nature Scientific Reports*, 4, doi: 10.1038/srep05848, 2014.
- 41 Sigl, M., Fudge, T. J., Winstrup, M., Cole-Dai, J., Ferris, D., McConnell, J. R., Taylor, K. C.,
42 Welten, K. C., Woodruff, T. E., Adolphi, F., Bisiaux, M., Brook, E. J., Buizert, C., Caffee, M.

1 W., Dunbar, N. W., Edwards, R., Geng, L., Iverson, N., Koffman, B., Layman, L., Maselli, O.
2 J., McGwire, K., Muscheler, R., Nishiizumi, K., Pasteris, D. R., Rhodes, R. H., and Sowers,
3 T. A.: The WAIS Divide deep ice core WD2014 chronology - Part 2: Annual-layer counting
4 (0-31 ka BP), *Clim. Past*, 12, 769-786, doi: 10.5194/cp-12-769-2016, 2016.

5 Udisti, R., Traversi, R., Becagli, S., and Piccardi, G.: Spatial distribution and seasonal pattern
6 of biogenic sulphur compounds in snow from northern Victoria Land, Antarctica, *Ann.*
7 *Glaciol.*, 27, 535-542, doi: 10.1017/S0260305500018024, 1998.

8